Bima Memoranda No. 45

BIMA ARRAY RESPONSE TO EXTENDED STRUCTURE

M. C. H. Wright
Radio Astronomy laboratory, University of California, Berkeley, CA, 94720

ABSTRACT

The BIMA 9-antenna array provides resolutions 5″, 2″, and 0.5″ in three standard array configurations at 100 GHz. Source structures more extended than a few times the synthesised beam width are attenuated and distorted in the synthesised images; structures larger than about 10 times the beam are not detected. We propose to add a more compact D array configuration with a resolution 17″ and better sensitivity to larger structures. Mosaicing observations using this D array configuration are discussed.

1. BIMA ARRAY CONFIGURATIONS

The BIMA Millimeter array presently consists of nine 6.1m diameter antennas which are arranged along an approximately T-shaped track with an East-West and a North-South extent of about 1km. The 9-antenna array is similar to that described by Welch etal. (1996) for the planned 10-antennas. Three standard array configurations provide resolutions of about 5″, 2″, and 0.5″ at 100 GHz. The synthesised beam response depends on the declination and hour angle coverage, as well as on the weighting of the uv-data. Figure 1 shows the synthesised beams at declination -30, -5, 15, and 45 degrees for uniform weighting of the uv-data with an hour angle range -4 to 4 hours, and an elevation limit 15 degrees. At high declinations the beams are roughly circular; at low declinations the beams are larger in declination; whilst at declinations close to the equator the sidelobe response is larger. The synthesised beams for other array configurations, HA ranges, declinations, and weighting of the uv-data are readily obtained using the MIRIAD script **beamgen**.

The most compact C array includes antennas separated by only 7.5m, so that, even at high declinations where there is little foreshortening of the baselines, the shortest possible baselines are sampled for the 6.1m antennas. The C array is sensitive to structure sizes up to about 60″ at 100 GHz. The B array is sensitive to structure sizes up to about 20″, and for the A array structures larger than about 6″ are not detected. For each configuration, the larger scale structures may be badly distorted and reduced in brightness due to the poorly sampled low spatial frequencies which have high visibility amplitudes. The response to large scale structure depends on the declination,

the hour angle coverage, the weighting of the uv-data, and the detailed source structure. A cleaner image of the compact source structure may be obtained by omitting the low spatial frequencies which are poorly sampling the extended source structure. Even in the C configuration the sensitivity to large structures is poor since few of the baselines sample low spatial frequencies. In order to provide better sensitivity and sampling for more extended structures we propose to add a D array configuration with 10 closely spaced antennas. This array will be most useful for high source elevations where the antennas are not shadowed. The synthesied beam for a proposed D configuration is shown in Figure 2 for declination 30 and 4 hours of uv-data about transit. This array has a resolution around 17″ and the sensitivity of a 30m antenna (assuming 70% aperture efficiency for the BIMA antennas and 30% for a 30m antenna at 3mm wavelength).

2. RESPONSE TO EXTENDED STRUCTURE

There are various ways of understanding the response of an interferometer array to extended source structure. An interferometer array samples the Fourier transform of the source brightness distribution between an inner limit, r_{uv}, ultimately set by the antenna diameter, and an outer limit set by the maximum antenna spacing, R_{uv}. If we model this as a uniformly sampled region with a hole in the center, then the missing information on the image is the source distribution convolved by a beam (FWHM $\sim \lambda/r_{uv}$) corresponding to the hole. The inner limit determines the response to large scale structure. The outer limit determines the resolution (FWHM $\sim \lambda/R_{uv}$). The distribution of the projected antenna spacings determines the sensitivity to structures between these two limits. Wilner & Welch (1994) give analytic expressions for the central brightness for Gaussian and uniform disk sources. For a disk distribution the central brightness can be negative. The integrated flux density may also be difficult to estimate. For interferometer observations where the zero spacing is missing, the integral over the whole image is zero. Thus the positive source brightness must be balanced elsewhere on the image by negative regions. The depth of these negative regions will vary with the image size. The integrated flux density for a Gaussian source at 45 degrees declination is shown in Figures 3–5 for each of the 3 array configurations. For the smallest Gaussian sources the flux density is fully recovered using either uniform or natural weighting of the uv-data. For more extended sources the images are distorted, and the integrated flux density in the image is progresively reduced as the source size increases. For larger sources, natural weighting of the uv-data, which does not overweight the larger uv-spacings, recovers more of the source flux density. The images obtained with other uv-sampling and source distributions can be readily obtained using the MIRIAD script **beamgen2** which prompts the user for a model source distribution and plots the synthesised and cleaned images, and the integrated flux density as a function of radius. Methods for estimating the integrated flux density of an extended source are discussed in BIMA memo 9.

3. SAMPLING LARGE SCALE STRUCTURE

There are several ways to sample large source structures. The first uses a single dish to sample the region of interest. This data can be combined with the interferometer image either in the image domain or in the uv-data. Single dish and interferometer images can be simply combined as a weighted average which can be deconvolved using the weighted average beam. This ignores the primary beam weighting in the interferometer image. Combination of the uv-data offers more control of the relative weighting and resulting beam shape for the combined data. This method is described by Vogel etal (1984); basically, the single dish data are deconvolved, multiplied by the interferometer primary beam pattern for each pointing center, and re-sampled in the Fourier domain to provide the missing spatial frequencies. The combined interferometer and single dish uv-data are then imaged in the usual way.

A second method is to use a more compact interferometer array, and combine the uv-data. This can also be done if the arrays have different primary beams (Wright etal, 1993). A tutorial script using MIRIAD tasks is available for combining data from different instruments.

The most serious defect is often an estimate of the total flux. An estimate of the zero-spacing flux can be added directly in a MEM deconvolution. Alternatively one can generate randomly sampled uv points including a zero spacing with the desired flux density estimate using the tasks **uvrandom** and **uvmodel**.

Another way of estimating spacings smaller than the minimum antenna spacing is to observe the source with multiple pointing centers. This is possible because an interferometer spacing D, actually includes spacings from D-d to D+d, where d is the antenna diameter. Short spacings can be estimated by a Fourier transform w.r.t. pointing center (Ekers & Rots, 1979; Cornwell, 1988).

The images from different pointings can be combined in a weighted average to form a composite, linear mosaic image using the MIRIAD task **linmos**. An elegant way to recover the large scale structure is to combine the data from different pointings before or during the deconvolution (Cornwell, 1988; Sault etal, 1996). The non-linear mosaic effectively recovers the short spacings included in the multiple pointings. Methods for sampling large scale structure are discussed in more detail in BIMA memo 35.

4. MOSAICING

For sources which are large compared with the primary beam, mosaicing provides a more uniform sensitivity. A central pointing and a hexagonal pattern at the primary beam half-power points samples the central point for 1/7 of the time at full power and 6/7 of the time at half-power, giving a sensitivity 0.84 compared with a single pointing center. At the half-power points the sensitivity is 0.70 compared with a single pointing at each position, assuming of course that the slew time is small compared with the integration time at each position. By similar arguments,

adding a second ring of pointings at half-power spacings gives a sensitivity 0.51 at the center and half-power radius, and 0.43 at the FWHM.

We made a test of various mosaicing algorithms available in MIRIAD. See the mosaicing chapter of the ATNF Miriad manual available via http://wwwatnf.atnf.csiro.au/Software/Analysis/miriad. uv-data was generated for 30″ and 60″ Gaussian sources using a hexagonal pointing pattern with a central pointing and a hexagon pattern at 1′ centers. The 7-pointings were sampled using the proposed D array giving an angular resolution 17.6″ x 16.9″ at declination 30. We tried imaging Gaussians with a total flux density of 10 Jy and 1 Jy with a bandwidth 100 MHz, system temperature 300 K and 4 hours of uv-data about transit. The uv-data was imaged using the mosiac option in the task **invert** followed by a joint deconvolution using both CLEAN and MEM algorithms. For comparison with these images we also seperately imaged and combined the pointings using linear mosaicing of both the synthesised, and seperately deconvolved images. Finally we used a direct Fourier transform w.r.t pointing center (Ekers & Rots, 1979; Cornwell,1988) to generate more closely sampled uv-data which was then Fourier transformed and deconvolved using CLEAN.

The resulting images are compared in Figures 6 & 7. For a 30″ Gaussian, both the MEM joint deconvolution and the linear mosaic of seperately deconvolved images are good representations of the source distribution. The linear mosaic of the synthesised images, and the joint deconvolution using CLEAN show 40% sidelobes. Most of the flux density is recovered in the MEM joint deconvolution (Table 1). A simple CLEAN deconvolution of the central field gives as good a result as a mosaic of all 7 fields. In the direct Ekers & Rots Fourier transform, the small number of pointings leads to an image with hexagonal ears corresponding to the pointing pattern. For a 60″ Gaussian 10% sidelobes remain even on the best images. The total flux recovered is also smaller (Table 2). The integrated flux density as a function of radius is plotted in Figures 8 & 9. MEM has made a good guess at the total flux, but the flux is partially in an extended ring around the central peak. At lower signal-to noise this characterization of MEM is even more pronounced.

5. CONCLUSIONS

1. For a single pointing center source structures more extended than a few times the synthesised beam width are attenuated and distorted in the synthesised images; structures larger than about 10 times the beam are not detected.

2. The proposed D array configuration of ten 6.1m BIMA antennas gives a resolution 17″ and a sensitivity to larger structures similar to that of a 30m antenna at 3mm wavelength.

3. A hexagonal pattern of pointing centers provides a more uniform sensitivity than a single pointing for sources larger than half of the primary beam width. For larger sources more pointings can be added.

4. Non-linear mosaicing using Maximum Entropy deconvolution (MEM) is better at imaging large

structures than the CLEAN algorithm, but may still produce spurious artifacts in the images.

5. Users should proceed with caution when imaging large structures. Empirical tests provide a way of estimating the possible errors on these images.

REFERENCES

Cornwell, T. J. 1988, A&A, 202, 316.
Ekers, R. D., & Rots, A.H. 1979, in IAU Col. 49, *Image Formation from Coherence Functions in Astronomy* , ed. van Schooneveld, C. (Dordrecht:Reidel), p.61
Vogel, S.N., Wright, M.C.H., Plambeck, R.L, & Welch, W.J., 1984, ApJ. 283, 655.
Sault, R.J., Staveleey-Smith, L., & Brouw, W.N., 1996, A&A in press.
Welch, W.J., etal, 1996., The BIMA Millimeter Array. PASP 108, 93.
Wilner, D.J., 1994, BIMA memo 35.
Wilner, D.J., & Welch, W.J., 1994, ApJ 427, 898.
Wright, M.C.H., 1991, BIMA memo 9.
M.C.H.Wright, & R.J.Sault, 1993, ApJ, 402, 546.
M.C.H.Wright, S.Ishizuki, J.L.Turner, P.T.P.Ho, & K.Y.Lo, 1993, ApJ, 406, 470.

This preprint was prepared with the AAS LaTeX macros v4.0.

Table 1. Total Flux density recovered for 30'' Gaussian source.

Image	Total Flux	Maximum	Minimum	Method
gauss30	10.00	3.3	0.00	Gaussian source model.
cm4	10.15	2.51	-0.24	CLEAN deconvolution of the central field.
memcm	14.01	2.48	-0.01	Joint deconvolution using MEM.
moscm	-0.08	1.97	-0.54	Joint deconvolution using CLEAN.
linmap	-5.37	2.02	-0.55	Linear mosaic of "dirty" images.
lincm	10.22	2.51	-0.01	Linear mosaic of separately CLEANED images.
uvpnt	11.08	14.87	-5.13	Ekers & Rots Fourier transform and CLEAN.

Table 2. Total Flux density recovered for 60'' Gaussian source.

Image	Total Flux	Maximum	Minimum	Method
gauss60	9.99	0.83	0.00	Gaussian source model.
cm4	3.17	0.43	-0.05	CLEAN deconvolution of the central field.
memcm	9.13	0.49	-0.02	Joint deconvolution using MEM.
moscm	-0.01	0.24	-0.11	Joint deconvolution using CLEAN.
linmap	2.76	0.24	-0.11	Linear mosaic of "dirty" images.
lincm	3.04	0.39	-0.05	Linear mosaic of separately CLEANED images.
uvpnt	16.8	4.61	-0.91	Ekers & Rots Fourier transform and CLEAN.

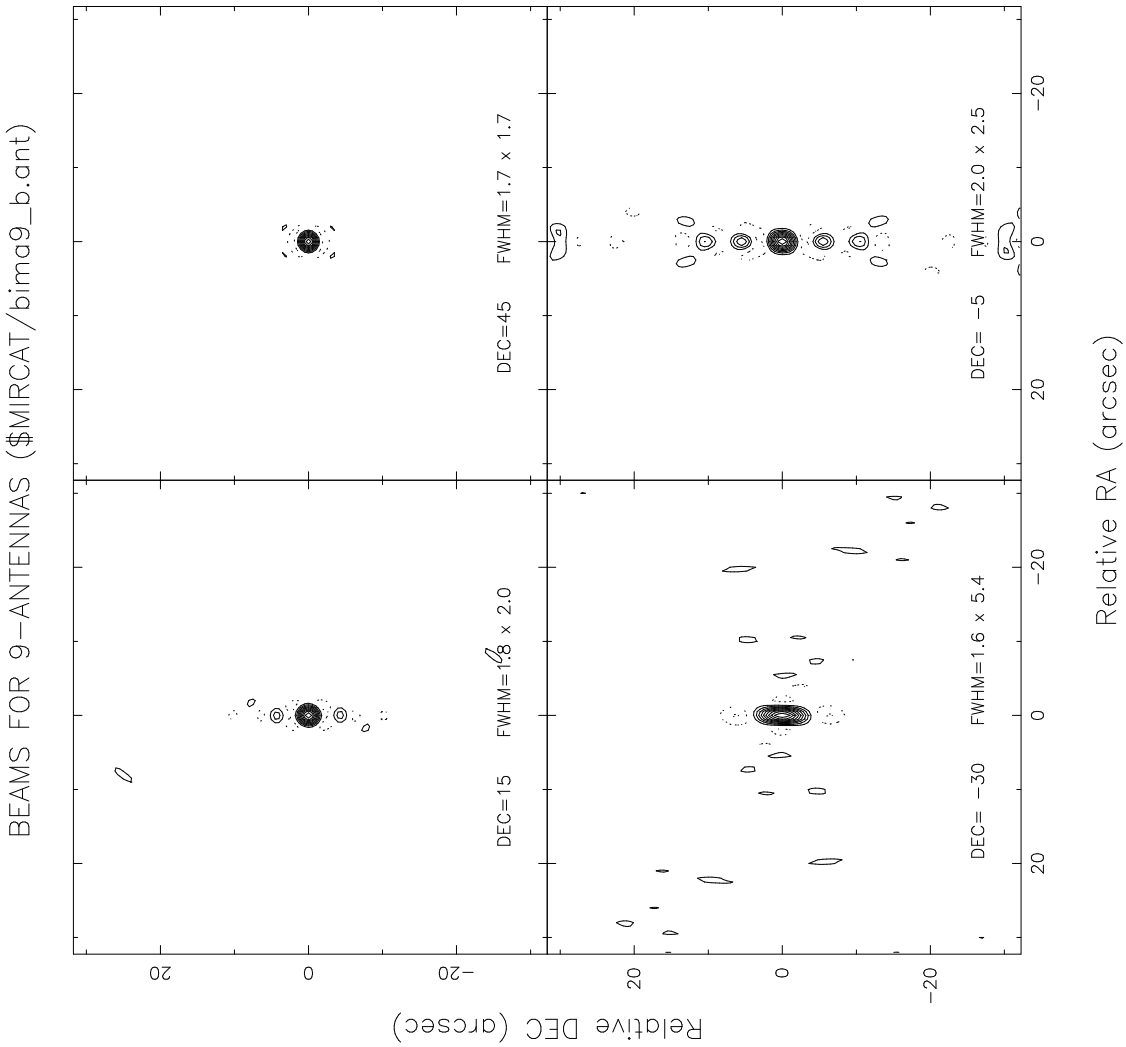

Fig. 1.— Synthesised beams for 9-antenna B array. Contour interval=0.1

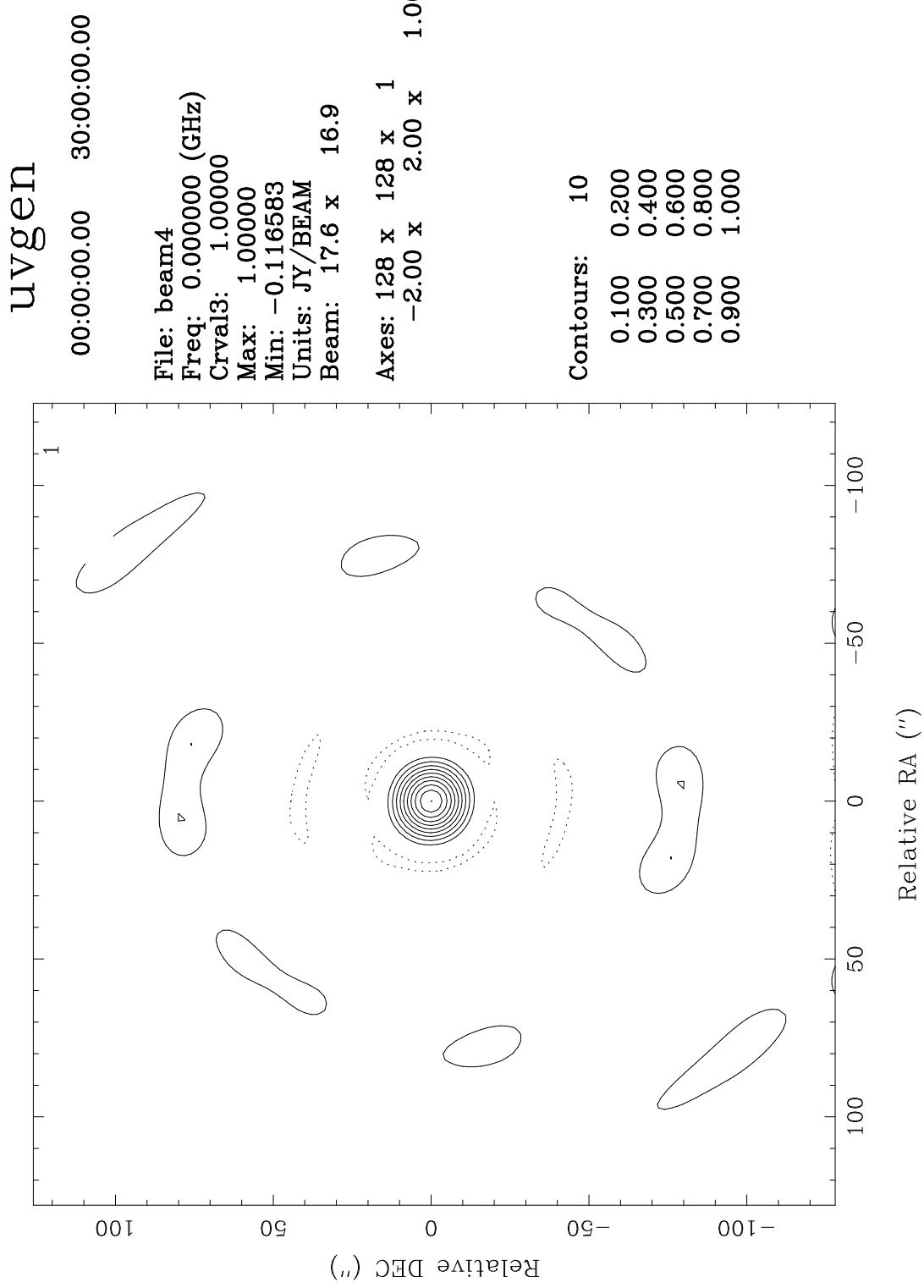

Fig. 2.— Synthesised beam for 10-antenna D array at DEC 30

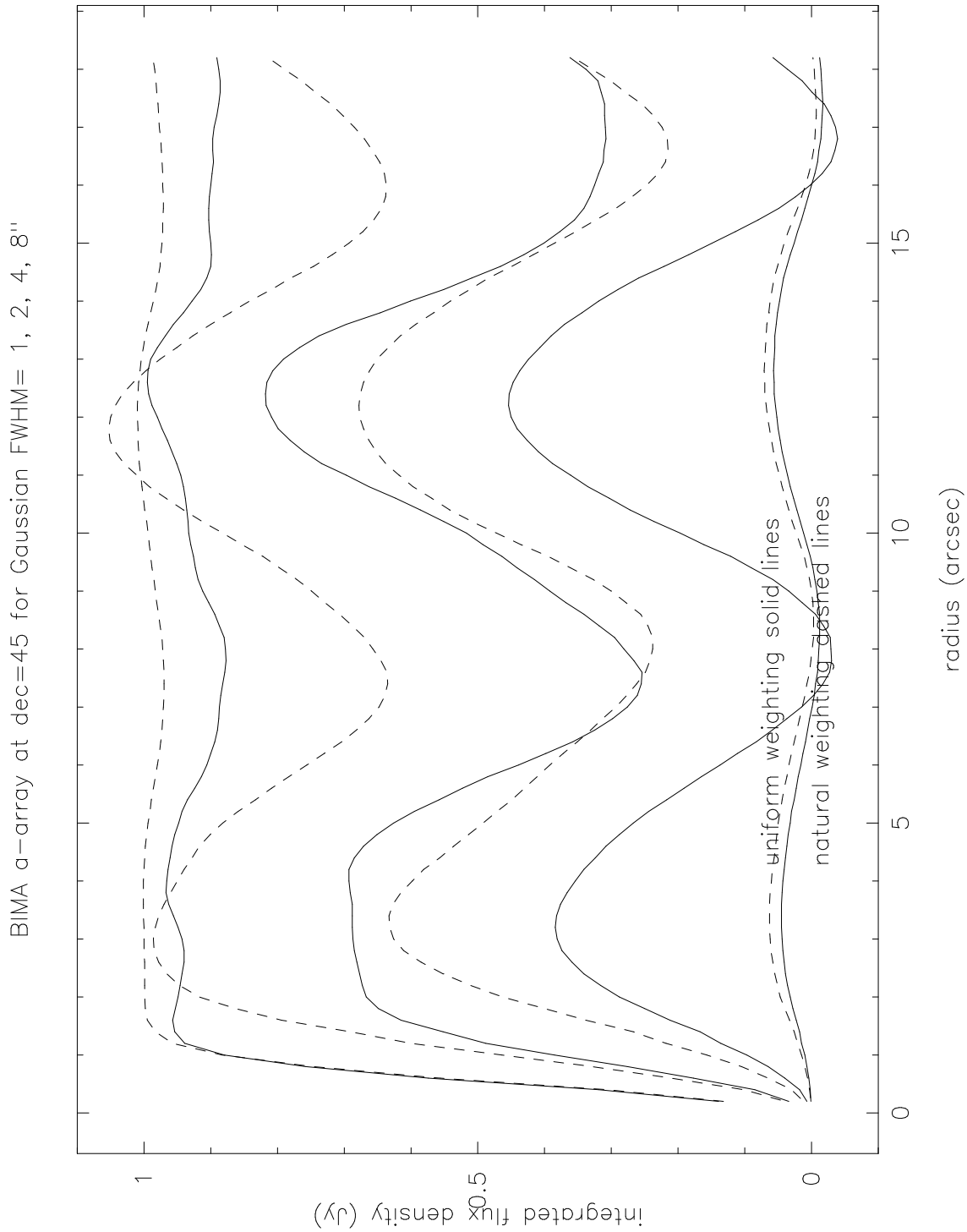

Fig. 3.— Integrated flux density for A array as a function of radius

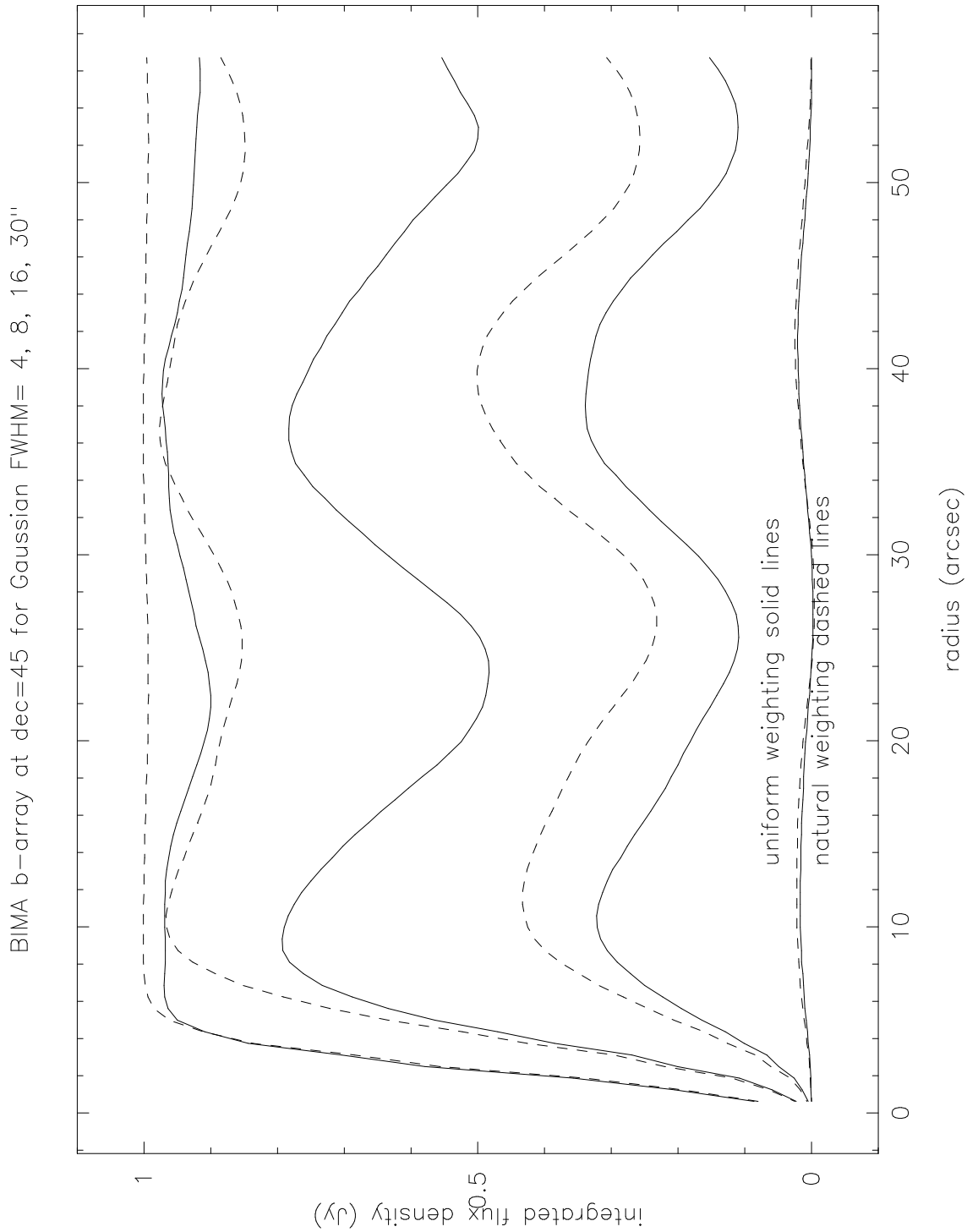

Fig. 4.— Integrated flux density for B array as a function of radius

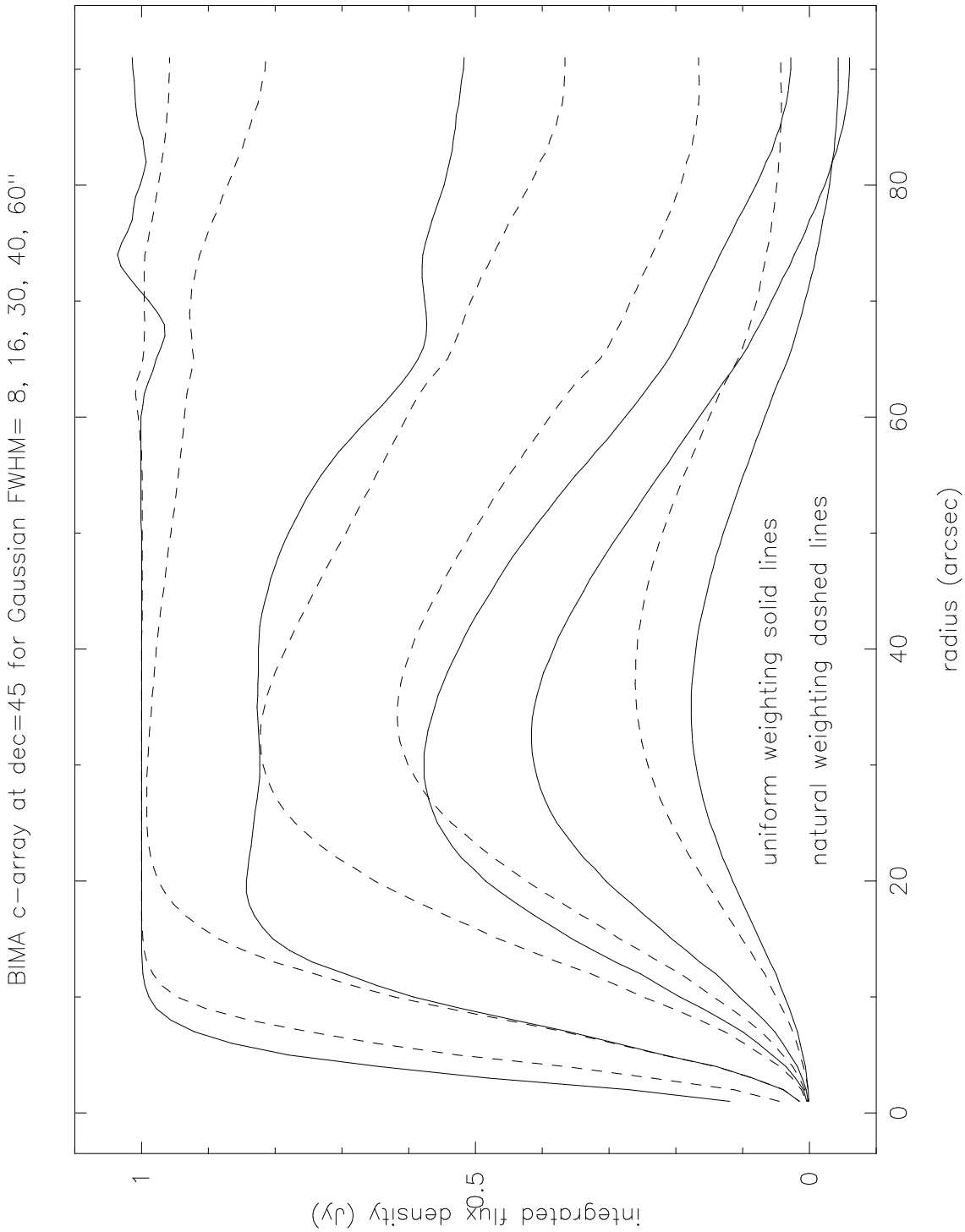

Fig. 5.— Integrated flux density for C array as a function of radius

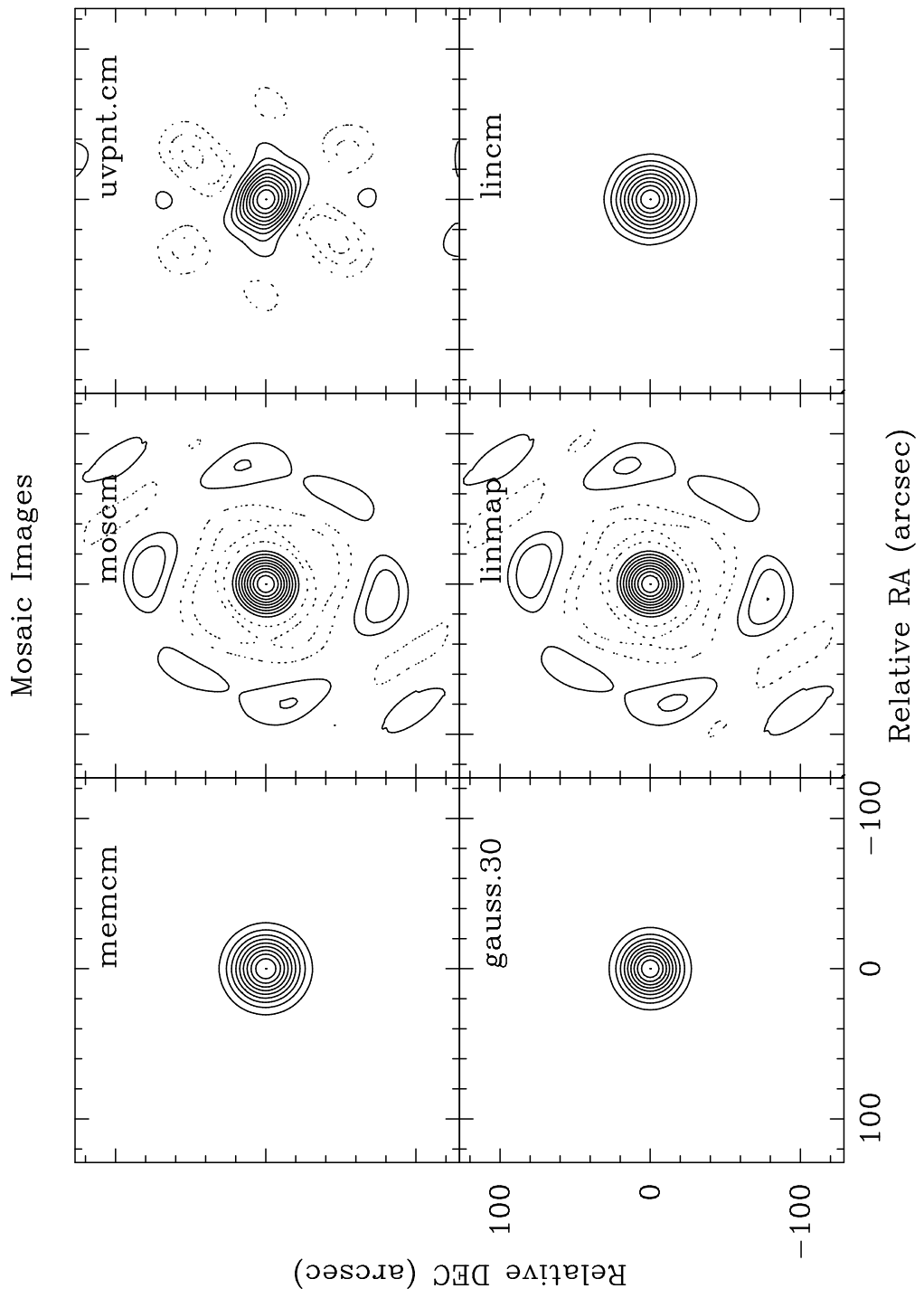

Fig. 6.— Mosaic images for 30″ Gaussian source using D array with 7 pointings

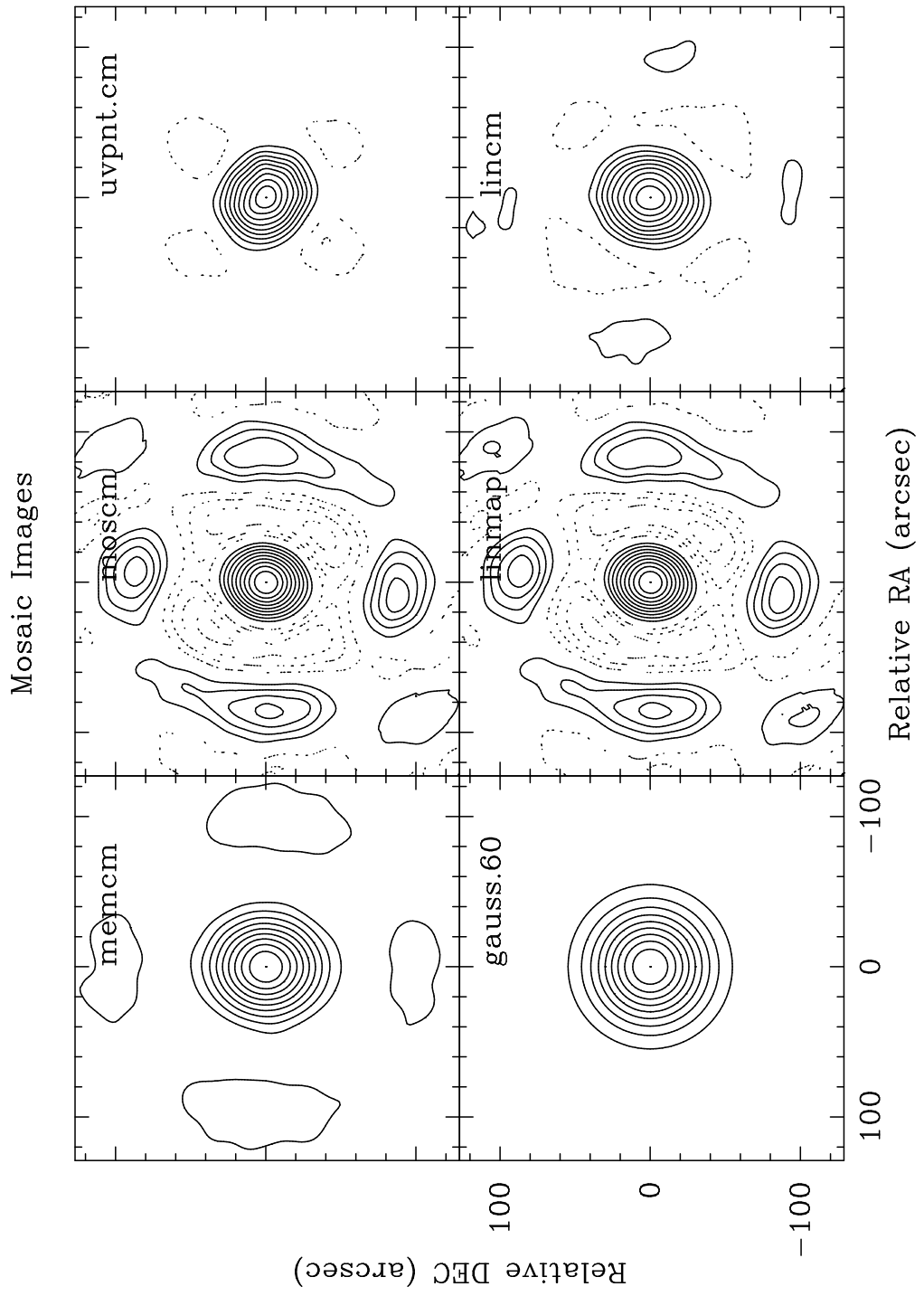

Fig. 7.— Mosaic images for 60″ Gaussian source using D array with 7 pointings

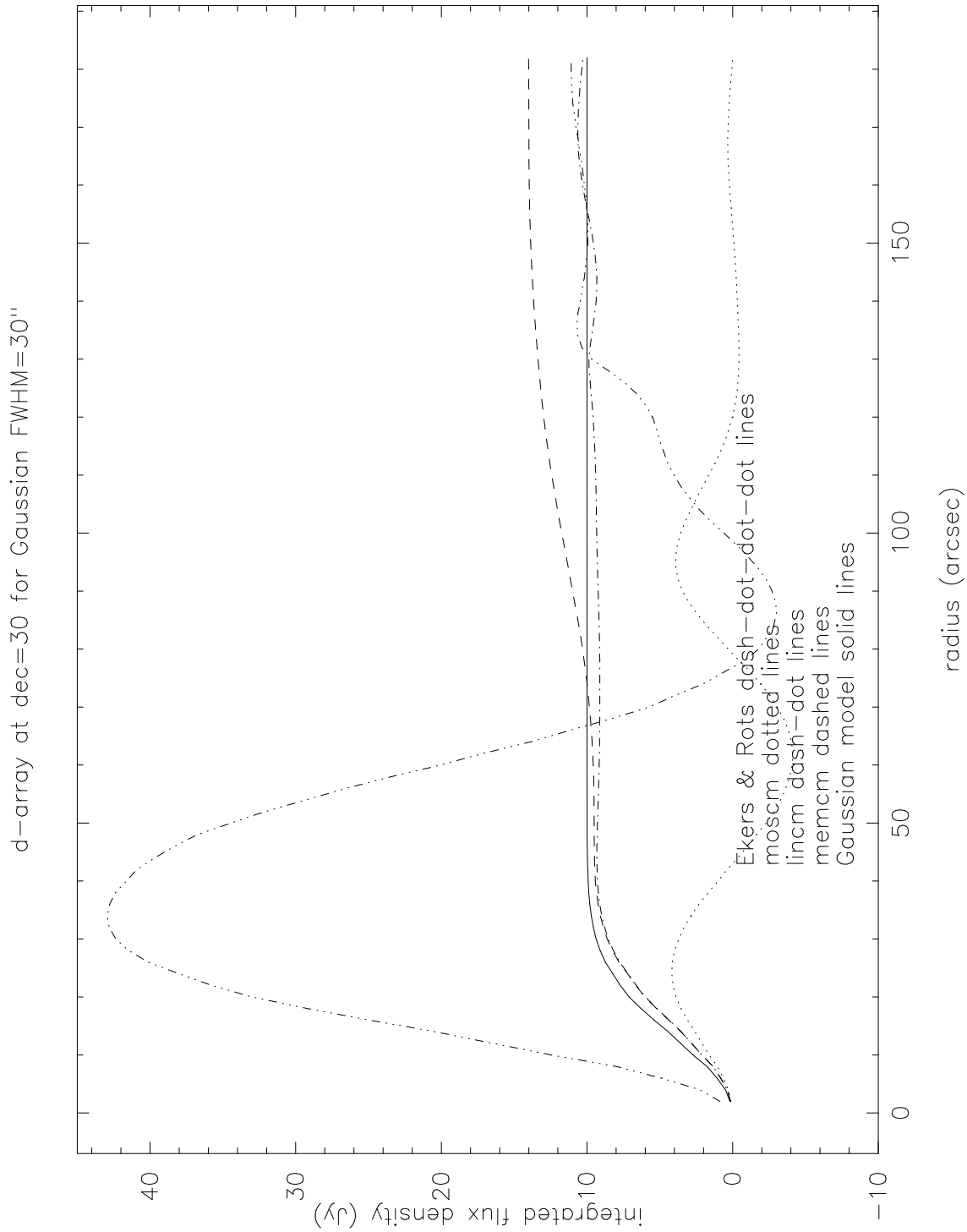

Fig. 8.— Integrated flux density for D array as a function of radius

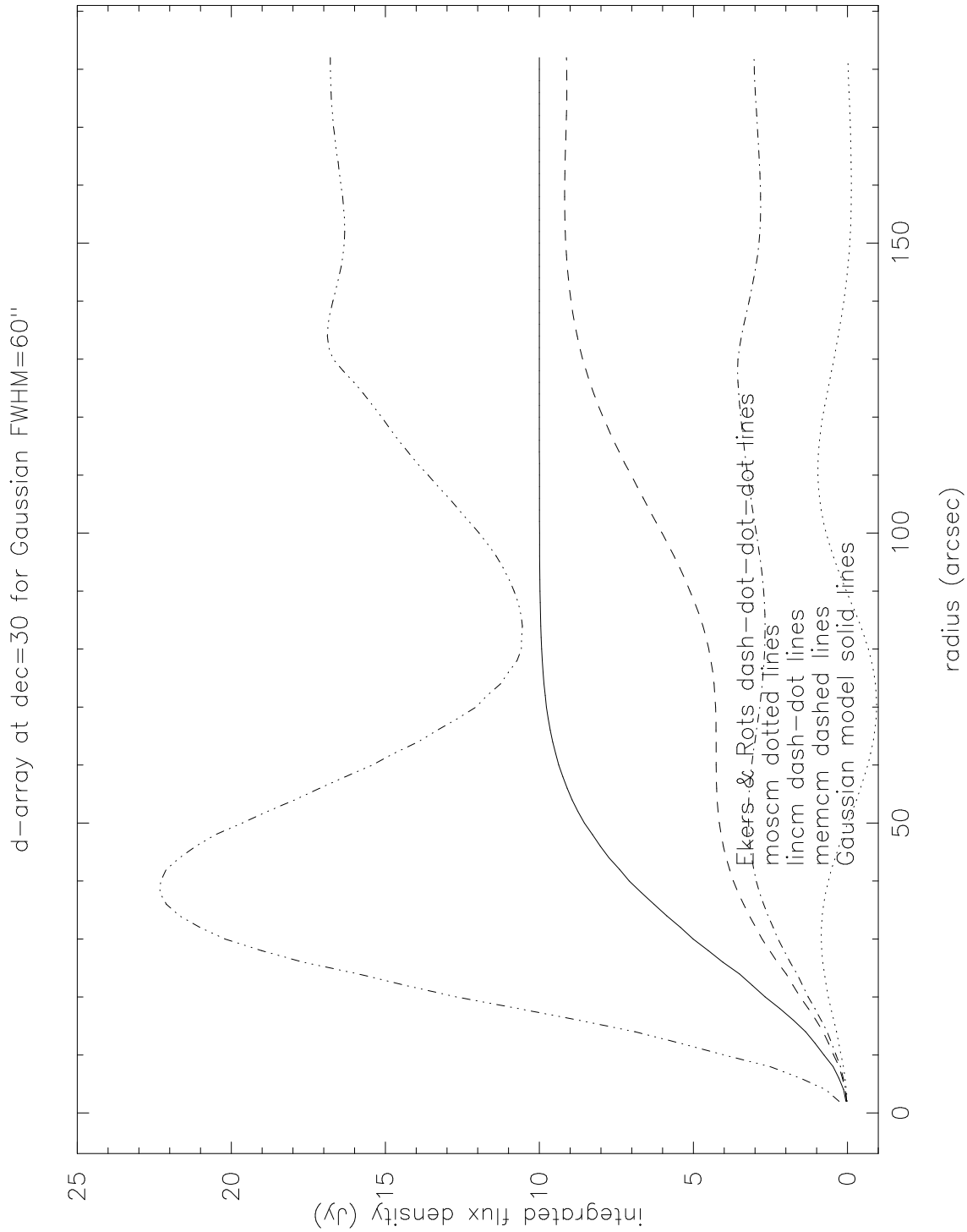

Fig. 9.— Integrated flux density for D array as a function of radius